Asymmetric Decline in Hydrological Efficiency of China's Natural and Planted Forests

Xiao Zhang[1,a] **, Xinxiao Yu** [a,b]**, Guodong Jia**[a,b,*]

[a] *School of Soil and Water Conservation, Beijing Forestry University, Beijing 100083, China*

[b] *Key Laboratory of State Forestry Administration on Soil and Water Conservation, Beijing Forestry University, Beijing 100083, China*

Corresponding author: Guodong Jia (jgd304304@126.com)

Abstract

The vegetation transpiration fraction (TF) is a key parameter linking terrestrial water and carbon cycles. Against the backdrop of global greening and climate change, the response of TF sensitivity to Leaf Area Index (LAI) changes (θ), and the relative roles of soil moisture (SM) and atmospheric drought (VPD), remain unclear, especially lacking a systematic comparison between China's Natural Forests (NF) and Planted Forests (PF). This study utilized multi-source datasets from 1990–2020 (including forest types, GLEAM, and ERA5-Land) and employed methods including sliding windows, partial correlation, ridge regression, and mediation effect models to systematically analyze the spatiotemporal dynamics of θ in NF and PF, and to quantify the independent contributions and dynamic shifts of SM and VPD. Results show: 1) Forest θ spatially increases from humid to semi-arid regions (NF > PF); temporally, θ shows a widespread significant decline, with PF declining more (mean of -0.262 %·m^{-2}·m^{2}·decade^{-1}) than NF, especially in semi-arid/semi-humid transition zones. 2) θ exhibits a "hump-shaped" nonlinear response to the joint SM-VPD gradient, peaking at moderate SM and medium-high VPD. 3) The key hydrological drivers of θ are undergoing a dynamic shift from "atmospheric demand" (VPD) to "soil supply" (SM); the independent control of SM (β_{SM}) has significantly strengthened over time, while that of VPD (β_{VPD}) has weakened. 4) The two forest types show distinct response mechanisms: NF is more sensitive to VPD, while PF is more sensitive to SM stress. Overall, China's forests are shifting towards a more "conservative" water-use strategy, and the enhancing effect of LAI on TF has significantly weakened under strengthening SM constraints and VPD stress. The differentiated high sensitivity—NF to atmospheric drought and PF to soil drought—provides critical insights for forest water

resource management and afforestation planning under future climate change scenarios.

Keywords:

natural forest, plantation forest, transpiration, leaf area index, soil moisture, vapor pressure deficit

1. Introduction

Terrestrial ecosystem evapotranspiration (E) is the primary pathway for land surface moisture to return to the atmosphere, playing a central role in the global water cycle (Liu et al., 2023; Sun et al., 2022). E comprises soil evaporation (Es), vegetation canopy interception (Ei), and plant transpiration (T) (Niu et al., 2020; Wei et al., 2017). Among these, vegetation transpiration, which transports water to the atmosphere through plant stomata, accounts for over 60% of total terrestrial E (Li et al., 2024; Wei et al., 2017). As transpiration is coupled with carbon assimilation and energy exchange, the vegetation transpiration fraction (TF, defined as T/E) quantifies the contribution of vegetation to land-atmosphere water vapor flux and is a key indicator of vegetation-climate coupling strength (Schlesinger and Jasechko, 2014; Wei et al., 2017). Understanding changes in TF is crucial for revealing ecohydrological mechanisms and predicting climate change impacts.

Persistent climate warming and rising atmospheric CO_2 over the past few decades have driven global vegetation greening and altered ecosystem water balances (Denissen et al., 2022; Hu et al., 2023). The increase in Leaf Area Index (LAI) directly enhances canopy interception and transpiration potential—global plant T is estimated to have increased by about 6% from 1990–2020, primarily attributed to LAI enhancement (Chen et al., 2024). However, the positive effect of LAI on transpiration is dependent on water availability: when soil moisture (SM) is scarce or atmospheric drought (often represented by Vapor Pressure Deficit, VPD) intensifies, plants regulate stomata to suppress water loss, thereby reducing transpiration and photosynthesis (Liu et al., 2020; Zahra et al., 2023). SM represents the supply-side constraint, while VPD represents the atmospheric demand-side pull; these two factors often co-vary and impose compound stress on ecosystems (Song et al., 2024). High VPD induces partial stomatal closure to prevent excessive water loss and hydraulic failure, causing transpiration rates per unit leaf area to saturate or even decline at high VPD (Grossiord et al., 2020; Novick et al., 2016). Therefore, even if LAI increases, the additional leaf area struggles to further increase T under extreme atmospheric drought (Xu et al., 2023).

https://doi.org/10.5194/egusphere-2025-5821
Preprint. Discussion started: 4 December 2025

Conversely, under moderate SM and some atmospheric demand, vegetation has both sufficient water and high evaporative demand, maximizing water-carbon exchange efficiency; it is then that LAI increases most effectively boost TF (Liu et al., 2020). During extreme soil drought, increased surface sensible heat further dries the near-surface atmosphere, creating a positive SM–VPD feedback that accelerates drought evolution (Qing et al., 2022; Zhou et al., 2019). Thus, accurately understanding the response of TF to LAI changes requires considering the synergistic effects and nonlinear impacts of both soil supply and atmospheric demand within a unified framework (Koehler et al., 2023). In recent years, discrepancies have existed regarding the relative roles of SM and VPD: some studies emphasize that atmospheric drought is more critical in limiting ecosystem water-carbon cycles (Novick et al., 2016); however, others, after decoupling their coupled effects, find that soil moisture is the dominant factor, especially in semi-arid regions where SM imposes a stronger limitation on productivity (Liu et al., 2020). Overall, SM and VPD are often highly correlated, intricately co-influencing plant transpiration and productivity. Disentangling their independent roles remains a challenge and a focal point in ecohydrological research.

Since the 1970s, China has implemented the world's largest-scale afforestation and ecological restoration projects, increasing forest cover from about 12% in the 1970s to over 22% currently (Cheng et al., 2025). China's current forests consist of vast newly planted and secondary forests, with a unique coexistence and distribution of Natural Forests (NF) and Planted Forests (PF): NF are mainly concentrated in the mountains of the Northeast and Southwest, characterized by complex age structures and deep-rooted species; PF are widespread in the plains and hills of the East, Central, and South, often with high density, single species, shallower roots, and subject to management activities like thinning and harvesting. These differences in origin, structure, and water-use strategies may lead to significant disparities between NF and PF in soil water acquisition, stomatal regulation, and hydraulic safety margins, consequently manifesting as different responses in LAI-induced TF changes (i.e., LAI–TF sensitivity, denoted as θ herein). This scientific question is not only related to deepening the understanding of vegetation water-use mechanisms but is also closely linked to regional water resource management, afforestation benefit assessment, and climate-adaptive forestry strategies. However, systematic research on this issue is currently lacking. Existing literature mostly discusses the sensitivity of transpiration or productivity under drought stress at

https://doi.org/10.5194/egusphere-2025-5821
Preprint. Discussion started: 4 December 2025

global or large regional scales (Liu et al., 2020; Novick et al., 2016) or focuses on ecohydrological processes in specific arid zones, but lacks a comparative assessment of θ characteristics across different forest types along a unified climatic gradient. Specifically: Are there systematic differences in θ between NF and PF along the climatic gradient from humid to semi-arid? How has this difference evolved over the last 30 years? In the context of coupled SM and VPD changes, which factor has a more significant independent control on θ, and has this dominance shifted due to different climatic backgrounds or decadal changes? Through which hydrological pathways (SM and/or VPD) do macro-climate changes (e.g., radiation, precipitation, temperature, wind speed) indirectly affect θ? Answering these questions will fill current research gaps and help deepen our understanding of forest-water relations in the context of climate change.

Our objective is to address these scientific questions by quantitatively analyzing the spatiotemporal patterns and climatic driving mechanisms of transpiration sensitivity (θ) in China's NF and PF from 1990–2020. To this end, we integrated multi-source data from remote sensing inversions and reanalysis products to extract growing season LAI, evapotranspiration components, and meteorological elements for pure NF and pure PF pixels at a 0.1° grid. First, we used the aridity index (AI) framework to divide the study area into humid, semi-humid, and semi-arid climatic zones to ensure comparability. Then, we employed multiple analytical methods: using 2D binning to construct the response surface of θ to the joint SM–VPD gradient at a national scale to extract the independent effects of SM and VPD; using a sliding window to calculate pixel-wise θ time series, and further using partial correlation and ridge regression models to quantitatively assess the independent contributions and trends of SM and VPD on θ's decadal changes; finally, introducing mediation effect models to decompose the impacts of large-scale climate factor changes on θ into indirect pathways via SM and VPD. All time-series trends were robustly estimated using the Theil–Sen slope and assessed with the Mann–Kendall test, ensuring consistency in result reliability and significance determination. This study will comprehensively reveal the spatiotemporal heterogeneity of transpiration sensitivity in China's different forest types and the dynamic shifts in their dominant controlling factors, providing new evidence for understanding the transformation of ecosystem water consumption behavior under a warming and greening background, and offering a scientific basis for future vegetation-water process modeling and climate-adaptive forest management.

2. Materials and methods

2.1. Data

We used datasets covering multiple aspects including forest type, vegetation physiology, and hydroclimate (Table 1). Forest type data were from the 1990-2020 spatial distribution dataset of planted and natural forests in China published by Cheng et al. (2024). This dataset, based on Landsat satellite imagery combined with extensive forest inventory plot data, used machine learning algorithms like random forest to finely classify forests nationwide, effectively distinguishing between PF and NF types. To match climate data, this dataset was upscaled to 0.1° resolution using Average Resampling, yielding the coverage degree of PF and NF within each 0.1° pixel. We defined pixels with a coverage degree equal to 100% as pure pixels for the corresponding forest type, and all subsequent analyses were conducted on these pure pixels. To ensure temporal consistency between climate data and forest type data, we adopted a dynamic matching strategy based on time periods. Considering the relatively slow change in forest cover and data availability, we divided the 1990–2020 study period into 7 time segments, selecting a representative year's forest type data for each segment as the masking benchmark for all years' climate data within that segment. The forest type maps for 1990, 1995, 2000, 2005, 2010, 2015, and 2020 were used as representative products for the periods 1990–1994, 1995–1999, 2000–2004, 2005–2009, 2010–2014, 2015–2019, and 2020, respectively.

LAI data were sourced from the GIMMS LAI4g dataset (https://www.gleam.eu/). It is generated based on GIMMS NDVI3g records from AVHRR satellite observations, inverted through a trained neural network model.

T, E, SM were from the Global Land Evaporation Amsterdam Model (GLEAM) v4.2 dataset. GLEAM 4.2a calculates terrestrial evapotranspiration fluxes using an improved hybrid physical–machine learning framework, dividing processes like rainfall interception, crop water demand, and soil moisture dynamics into serial modules, and assimilating satellite observations (e.g., microwave soil moisture, vegetation optical depth) and reanalysis forcing data. To ensure the robustness of E, T, and the subsequently calculated TF and θ results, we simultaneously introduced the Simple

Terrestrial Hydrosphere v2 (SiTHv2) product as an independent control. SiTHv2 (Zhang et al., 2024) is inverted from an ecohydrological energy balance model (Simple Terrestrial Hydrosphere) driven by reanalysis meteorology and constrained by satellite Vegetation Optical Depth (VOD). Our spatiotemporal comparison showed that the two products achieved moderate-to-high consistency in spatial patterns and interannual trends of TF and θ for both NF and PF (Fig. S1, S2), with regression slopes close to the 1:1 line and acceptable systematic bias, proving that the key conclusions of this study regarding TF and θ are robust to the data source.

Near-surface meteorological elements including pressure (Pa), relative humidity (RH), air temperature (Ta), precipitation (P), dewpoint temperature (Td), eastward and northward wind speed components (WSu, WSv), net radiation (Rn), and potential evapotranspiration (PET) were from the European Centre for Medium-Range Weather Forecasts (ECMWF) fifth-generation reanalysis (ERA5-Land, https://cds.climate.copernicus.eu/). It is generated through the advanced H-TESSEL land surface model, assimilating extensive ground and satellite observations globally, providing spatiotemporally continuous and physically consistent high-quality climate records.

Due to the temporal coverage limitations of the forest type data, all environmental variables were extracted for the growing season (April–October) from 1990–2020. Daily or monthly data were aggregated into growing season averages (e.g., Ta, VPD, SM) or cumulative values (e.g., E, T, P).

Table 1 Data overview

Variable	Data set	Resolution		Time span	References
		Spatial	Temporal		
Forests type	Planted and natural forest maps in China from 1990 to 2020	1 km	5 years	1990-2020	https://doi.org/10.1016/j.isprsjprs.2024.01.024
LAI	GIMMS_LAI4g	1/12°	15 day	1982-2020	https://doi.org/10.5194/essd-2023-68, in review, 2023
E, T, SM	GLEAM4.2a	0.1°	1 day	1980-2023	https://www.gleam.eu
Validation E, T	SiTHv2	0.1°	1 day	1982-2020	https://data.tpdc.ac.cn/en/data/bc51e1b0-494c-4cd5-ae4d-eba6b9d2322c

Ta, Pa, Td P, PET, Rn	ERA5-LAND	0.1°	1 month	1950-2025	https://doi.org/10.24381/cds.68d2bb30

LAI: Leaf area index; E: Evaporation; T: Transpiration; SM: Soil moisture; Ta: Air temperature; Td: Dewpoint temperature; Pa: Air pressure; P: Precipitation; PET: Potential evapotranspiration; Rn: Net radiation.

2.2. Study region

Our study area is terrestrial China, which spans temperate, subtropical, and tropical climate zones. The subjects are China's NF and PF. NF are mainly concentrated in the mountains of the Northeast and Southwest, while PF are widely distributed across the plains and hills of the East, Central, and South (Fig. 1a). The vast majority of NF and PF are located in humid and semi-humid zones (Fig. 2).

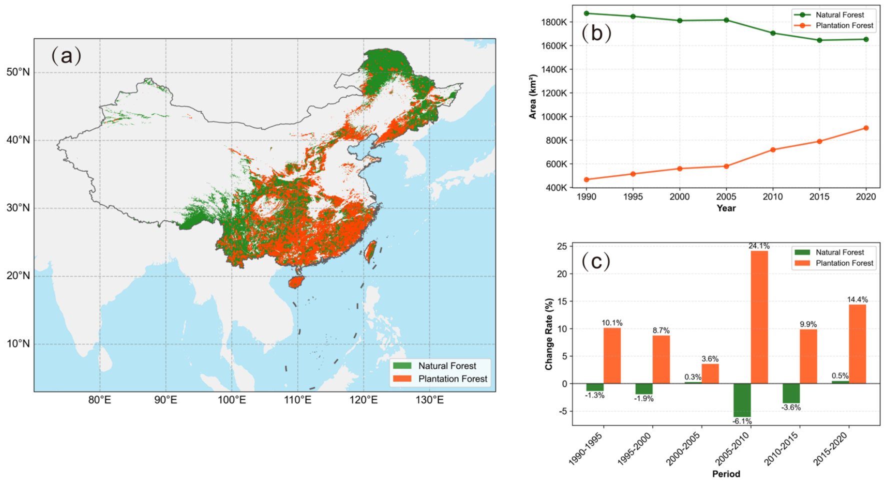

Figure 1 Spatiotemporal characteristics of China's Natural Forests (NF) and Planted Forests (PF) from 1990–2020. (a) Average spatial distribution of NF (green) and PF (orange) in China from 1990–2020. (b) Dynamic changes in the area (km²) of NF and PF from 1990–2020. (c) Rate of change (%) in NF and PF area for each five-year period from 1990–2020.

https://doi.org/10.5194/egusphere-2025-5821
Preprint. Discussion started: 4 December 2025

2.2.1. Aridity Index and Analytical Framework

We used the aridity index (AI) as the basis for classifying climatic backgrounds to construct a unified analytical framework. The index is defined as the ratio of annual potential evapotranspiration (PET) to annual precipitation (P) (AI = PET / P). We first calculated the multi-year mean AI spatial distribution map for 1990–2020, then divided China into four arid/humid zones: humid ($AI < 1$), semi-humid ($1 \leq AI < 1.5$), semi-arid ($1.5 \leq AI < 4$), and arid ($AI \geq 4$) (Zhu et al., 2022). This zoning scheme provided the geographical framework for all subsequent comparative analyses involving spatial heterogeneity (e.g., binning analysis, zonal statistics). Due to the extremely scarce forest samples in the arid zone, this zone was excluded from the statistical analysis to ensure the robustness of the results.

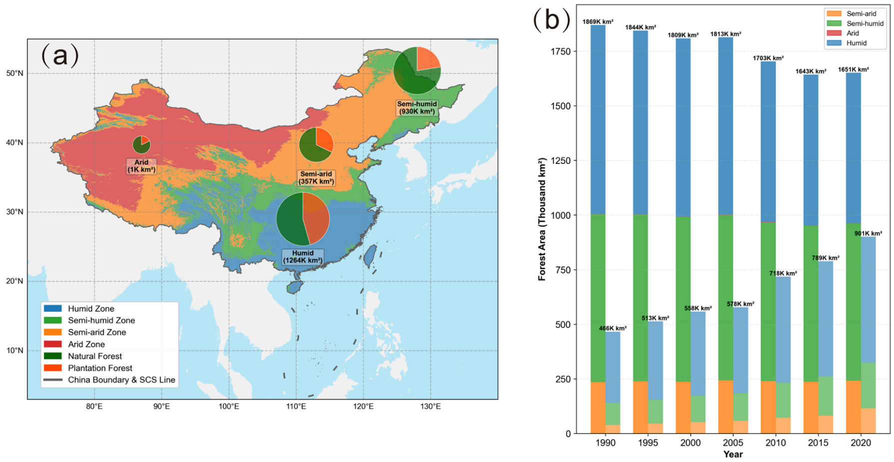

Figure 2 Spatiotemporal distribution and composition of forests in different climatic zones in China from 1990–2020. (a) Spatial distribution of the four climatic zones (humid, semi-humid, semi-arid, arid) in China; pie charts show the total forest area within each zone and its composition of natural forest (green) and planted forest (orange). (b) Dynamic changes in forest area in each climatic zone from 1990–2020; the value at the top of the bar represents the total national forest area (K km²) for that year.

2.3. Methods

2.3.1. VPD Calculation

Vapor Pressure Deficit (VPD, hPa) is expressed as the difference between saturation vapor pressure (P_s, hPa) and actual vapor pressure (P_w, hPa):

$$VPD = P_s - P_w \quad (1)$$

To calculate VPD, we used directly observed meteorological parameters, including air temperature (T_a, °C), relative humidity (RH, %), and air pressure (P_a, hPa). P_s was calculated using the improved Magnus equation (Yuan et al., 2019):

$$P_s = 6.112 \times f \times e^{\frac{17.67 \times T_a}{T_a + 243.5}} \quad (2)$$

where f is the atmospheric pressure enhancement factor, which corrects for the effect of pressure on saturation vapor pressure in moist air (Buck, 1981). This coefficient is calculated using P_a as follows:

$$f = 1 + 7 \times 10^{-4} + 3.46 \times 10^{-6} \times P_a \quad (3)$$

P_w is then derived from P_s and RH:

$$P_w = P_s \times RH \times \frac{1}{100\%} \quad (4)$$

2.3.2. Sensitivity of transpiration fraction to LAI

The sensitivity (θ, %·m^{-2}·m^{2}) of the transpiration fraction (TF, %) to LAI changes is expressed by the following formulas:

$$TF = \frac{T}{E} \times 100\% \quad (5)$$

$$\theta = \frac{\partial TF}{\partial LAI} \quad (6)$$

where T is vegetation transpiration (mm), and E is total surface evapotranspiration (mm). θ essentially reflects the average change in TF when LAI changes by one unit. To ensure computational accuracy, it is necessary to ensure that ΔLAI is not close to zero when deriving θ values. Therefore, when the LAI change trend within a specific time window fell in the -0.01 to 0.01 ($m^2\ m^{-2}\ decade^{-1}$) range, the relevant data were excluded from the analysis. We calculated two time-scales of θ. The full-period mean θ characterizes the average state from 1990–2020, derived by linear regression fitting of the annual growing season mean TF and LAI data from 1990-2020 to obtain a single θ value representing the average condition. The θ time series characterizes decadal changes, generated using an 11-year sliding window method to calculate θ within the window annually, creating a θ time series (1995-2015) marked by the window's center year, which was used for subsequent dynamic trend analysis.

2.3.3. Static Spatial Attribution: Binning Analysis

To quantify the independent contributions of SM and VPD to the spatial differentiation of θ, we used binning analysis. First, using all pure forest pixels in the study area as samples, we extracted their full-period mean θ, SM, and VPD, and Z-score standardized them. When assessing the independent effect of VPD, Δθ(VPD|SM), pixels were divided into bins based on SM values. Within each bin of similar SM, the difference in mean θ between high and low VPD groups was calculated. Finally, the differences from all bins were averaged to obtain the net effect of VPD after controlling for SM. The assessment of SM's independent effect, Δθ(SM|VPD), followed the same logic, binning by VPD and comparing high vs. low SM groups. This method spatially separates the independent contributions of the two factors using a "control variable" approach.

2.3.4. Dynamic Temporal Attribution: Partial Correlation and Ridge Regression

To investigate the control of SM and VPD on the temporal dynamics of θ at the pixel scale, we used partial correlation and ridge regression, both analyzing the 1995–2015 11-year sliding window time series data. This analysis had two levels: ① Static relationship analysis: First, for each pixel, we calculated an overall partial correlation coefficient and ridge regression coefficient using its complete 1995–2015 time series. This represents the average independent influence of SM and VPD on θ during this period. ② Dynamic trend analysis: To explore how this influence evolved, we applied a second-level sliding window analysis. Specifically, we used an 11-year window sliding over the 1995–2015 time series. Within each window, we calculated the partial correlation and ridge regression coefficients, thus generating a time series of the coefficients themselves for each pixel. Finally, we performed a trend analysis on this newly generated coefficient time series to reveal whether the independent influence or contribution of SM and VPD strengthened or weakened over time. The static relationship provides the full-period average independent impact, while the secondary sliding window tests whether these impacts evolved or underwent shifts; by treating the coefficients themselves as time series for trend estimation, we avoid masking heterogeneity from different periods within a single overall coefficient.

Partial correlation analysis: We calculated two partial correlation coefficients pixel-wise: $r(\theta, SM|VPD)$and $r(\theta, VPD|SM)$. The former represents the net correlation between θ and SM after removing the influence of interannual VPD fluctuations, indicating SM's independent influence; the latter similarly represents VPD's independent influence.

Ridge regression analysis: Considering the collinearity between SM and VPD, we further employed a ridge regression model ($\theta = \beta_1 \cdot SM + \beta_2 \cdot VPD$) to more robustly quantify their independent contributions. Ridge regression, by introducing an L2 regularization term, effectively addresses multicollinearity, making the regression coefficients (β) more stable and reliable. We performed the regression on standardized time series, so the resulting standardized coefficients (β_1 and β_2) directly reflect the relative importance of SM (β_{SM}) and VPD (β_{VPD}). Based on this, we also calculated the Relative Contribution (RC), e.g., $RC_{SM} = |\beta_1| / (|\beta_1| + |\beta_2|)$, to intuitively determine which factor was dominant at each pixel.

2.3.5. Mechanistic Attribution: Mediation Effect Analysis

To test the causal chain of macro-climate change impacting θ through local hydrological processes, we constructed a mediation effect model. The independent variable X was the climate factor trend (P, Ta, Rn, WS), the mediator variable M was the local water supply-demand status (SM and VPD trends), and the dependent variable Y was the θ trend. The model analysis yielded the indirect effect transmitted via M. The significance of all mediation effects was tested using Bootstrap resampling (1000 times).

2.3.6. Trend Analysis and Testing

In this study, all time series (including coefficient series from the 11-year sliding window) were uniformly analyzed using the Theil–Sen median slope estimation, and trend significance was assessed using the Mann–Kendall (MK) test (two-tailed, α=0.05). To avoid bias from temporal autocorrelation, the MK statistic was corrected using variance correction. This setup ensures robustness to outliers, accounts for temporal autocorrelation, and maintains consistency in trend determination.

https://doi.org/10.5194/egusphere-2025-5821
Preprint. Discussion started: 4 December 2025

3. Results

3.1. Spatiotemporal differentiation and trends of θ

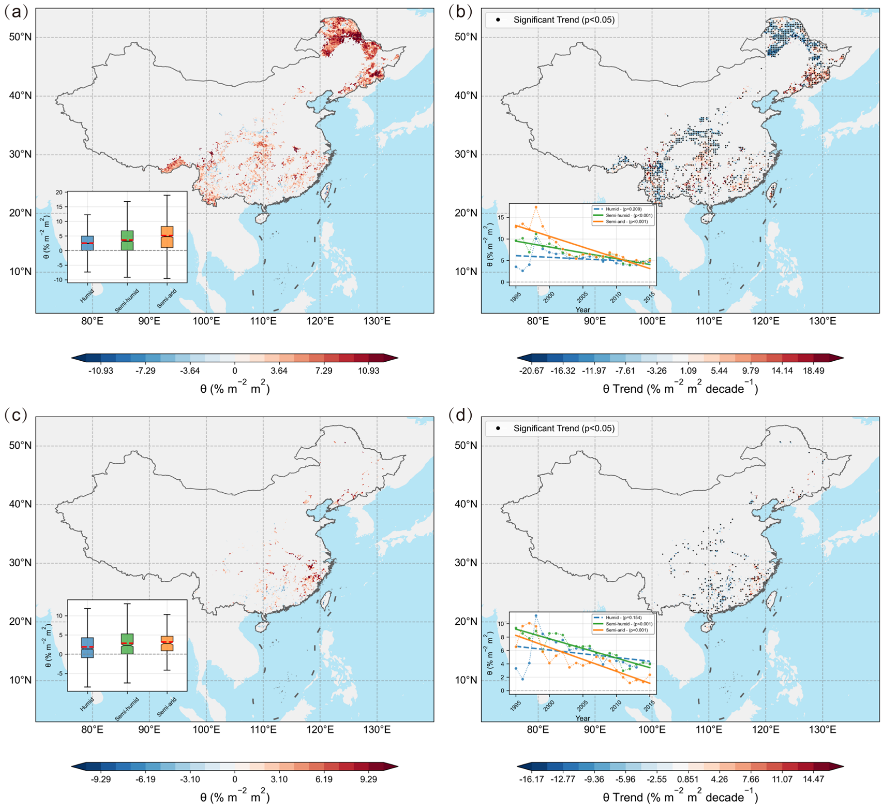

Figure 3 Spatiotemporal dynamics of LAI-TF sensitivity (θ) for China's Natural Forests (NF) and Planted Forests (PF) during the 1990-2020 growing season. (a) and (c) show the multi-year mean θ spatial distribution for NF(a) and PF(c) during the growing season (April-October) from 1990-2020. The bottom-left boxplots show the statistical distribution of θ values for both forest types in different climatic zones (Humid, Semi-humid, Semi-arid). (b) and (d) show the spatial distribution of the θ interannual change trend for NF(b) and PF(d) from 1990–2020. The trend ($\%\cdot m^{-2}\cdot m^{2}\cdot decade^{-1}$) is based on the θ time series calculated using an 11-year sliding window and estimated by the Theil–Sen slope. Black dots indicate significant trends ($p<0.05$) by the Mann–Kendall test. The bottom-left line plots show the spatially averaged θ interannual time series for each climatic zone, overlaid with linear trend lines (solid lines for significant trends, dashed for non-significant).

The multi-year mean θ spatially increases from the humid zone to the semi-humid and then to the semi-arid zone (Fig. 3a, 3c), with NF θ being significantly higher than PF θ ($p < 0.001$); this difference widens with increasing aridity. The high-value belt for NF is mainly concentrated in the semi-arid to semi-humid monsoon margin and ecological transition zones (e.g., North China, northern Loess Plateau, and western Northeast China). PF, though dispersed, shows relatively high values in the southeastern coast and the Northeast. θ exhibits a widespread significant decreasing trend during the study period (Fig. 3b, 3d), which is particularly prominent in the semi-arid and semi-humid transition zones ($p < 0.001$), while the humid zone is relatively stable. Although NF has a higher initial θ, PF shows a larger average decline (approx. −0.262 vs. −0.142 %·m^{-2}·m^2·$decade^{-1}$). Pixels with significant decline largely overlap with the initial high-value areas, suggesting a systematic weakening in these sensitive zones over the past 30 years.

3.2. Control of Water Stress Factors (SM and VPD) on θ

3.2.1. Response Pattern of θ to the SM-VPD Joint Gradient

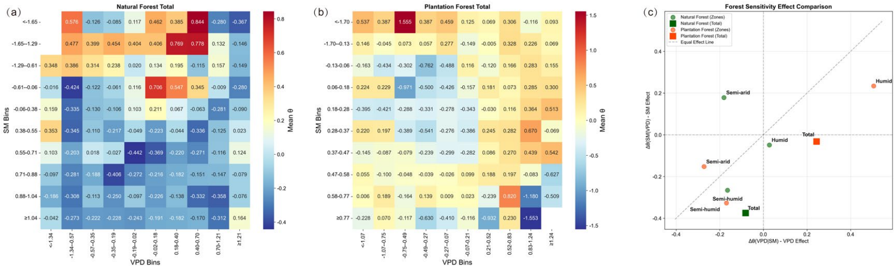

Figure 4 Pooled spatial analysis and independent effect comparison of forest LAI—TF sensitivity (θ) under the SM-VPD joint gradient for the 1990-2020 growing season. (a) Natural Forest (NF), (b) Planted Forest (PF): All pure forest pixels were binned into 10×10 bins based on SM and VPD deciles. Each cell shows the mean θ for that bin (only bins with sample size ≥10 are shown). (c) Independent effect comparison: Within each SM bin, the difference in mean θ between the top 20% and bottom 20% VPD groups was averaged across bins to get Δθ(VPD|SM); similarly, Δθ(SM|VPD) was derived by comparing SM groups within each VPD bin. Circles represent arid/humid zones, squares represent the national total; the dashed line is the 1:1 line (Δθ(VPD|SM)= Δ θ(SM|VPD). (θ is dimensionless if Z-score standardized).

To explore the universal impact patterns of SM and VPD on θ, we first pooled all forest pixels nationally via binning analysis to construct a response surface of θ to the 2D SM-VPD environmental gradient. θ is suppressed at extreme SM and VPD values but peaks under moderate SM and medium-high VPD conditions, forming a "hump-shaped" response pattern (amplified in the middle, attenuated at the extremes) (Fig. 4a, b). The independent effect comparison further shows (Fig. 4c) that in the semi-arid zone, Δθ(SM|VPD) is significantly greater than Δθ(VPD|SM), meaning SM is the dominant factor for θ changes. In the humid zone, VPD's relative importance increases significantly, with the semi-humid zone showing transitional characteristics. In the type comparison, NF exhibits a higher peak and a broader sensitive range in most SM-VPD combinations, while PF shows a narrower response window and earlier sensitivity attenuation (lower θ in high/low-end bins), suggesting PF has a weaker marginal response to extreme wet or dry—high VPD conditions.

3.2.2. Dynamic Evolution of SM and VPD Independent Control

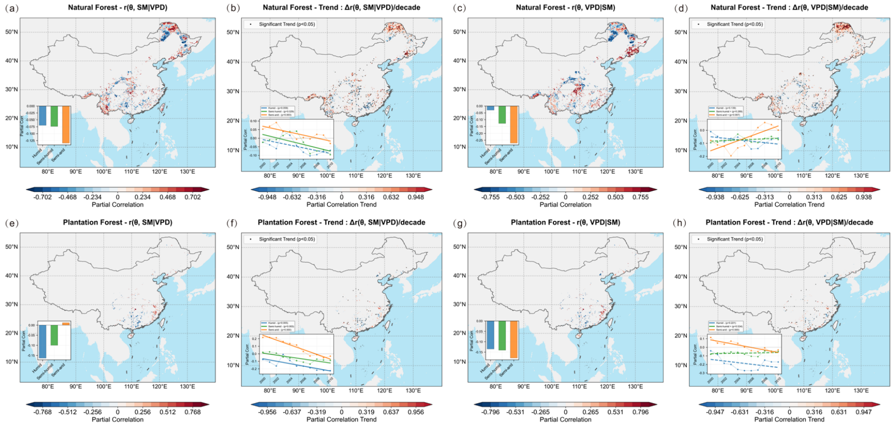

Figure 5 Partial correlation of forest LAI-TF sensitivity (θ) with SM/VPD and its decadal trends. (a) NF r(θ, SM | VPD) spatial distribution; (b) NF Δr(θ, SM | VPD) trend (change per decade); (c) NF r(θ, VPD | SM); (d) NF Δr(θ, VPD | SM) trend; (e–h) corresponding results for PF. Partial correlation coefficients reflect the linear association strength between θ and the target variable after controlling for the other variable. Trends were estimated using Theil–Sen slope, significance by Mann–Kendall test, with black dots marking p<0.05. Inset bar plots show mean partial correlation coefficients for arid/humid zones; inset line plots show temporal trends of spatially averaged partial correlation coefficients for each climatic zone, overlaid with linear trend lines (solid for significant, dashed for non-significant).

https://doi.org/10.5194/egusphere-2025-5821
Preprint. Discussion started: 4 December 2025

Based on the θ from the sliding window (1995–2015), the independent effects of SM and VPD on θ are predominantly negative. The national average for NF was r(θ, SM|VPD) = −0.079 and r(θ, VPD|SM) = −0.105. PF's negative correlation was stronger, at r(θ, SM|VPD) = -0.1412 and r(θ, VPD|SM) = -0.1388. Spatially, negative correlation areas are mainly in Southern China, while positive correlation areas are concentrated in the Northeast (Fig. 5a, c).

The two forest types show different dependencies on the arid/humid gradient. For NF, the negative control of both SM and VPD gradually weakens from the semi-arid to the humid zone, with the VPD effect being particularly obvious (mean r(θ, VPD|SM) weakens from -0.2710 in the semi-arid zone to -0.0294 in the humid zone). This indicates that in humid regions, NF sensitivity (θ) is largely unaffected by VPD's independent influence. However, PF shows the opposite pattern: its sensitivity (θ) is under stronger negative constraint from both SM and VPD in humid regions (means -0.1632 and -0.1351, respectively), while in the semi-arid zone, SM's independent influence even turns slightly positive (mean 0.0118) (Fig. 5e, g inset plots).

The negative control of SM (i.e., r(θ, SM|VPD)) shows a negative trend (Δr<0) in most of Southern China, meaning the negative correlation is strengthening; this phenomenon is particularly prevalent in PF (Fig. 5b, f). In contrast, the control of VPD (i.e., r(θ, VPD|SM)) shows a widespread weakening trend (positive trend) nationally. Large areas of significant positive trends appear in both NF and PF in Eastern and Southern China (Fig. 5d, h). The time-series analysis (inset plots) clearly reveals that in humid and semi-humid regions, the negative correlation of SM's influence deepens over time (trend line slopes down), while the negative correlation of VPD's influence gradually weakens, even turning positive (trend line slopes up). This "one strengthens, one weakens" dynamic evolution reveals that the forest's response pattern to water stress may be undergoing a systematic shift—from being more constrained by atmospheric drought (VPD) in the past to being more constrained by soil drought (SM) today.

3.2.3. Quantification and Spatiotemporal Heterogeneity of Dominant Hydrological Drivers

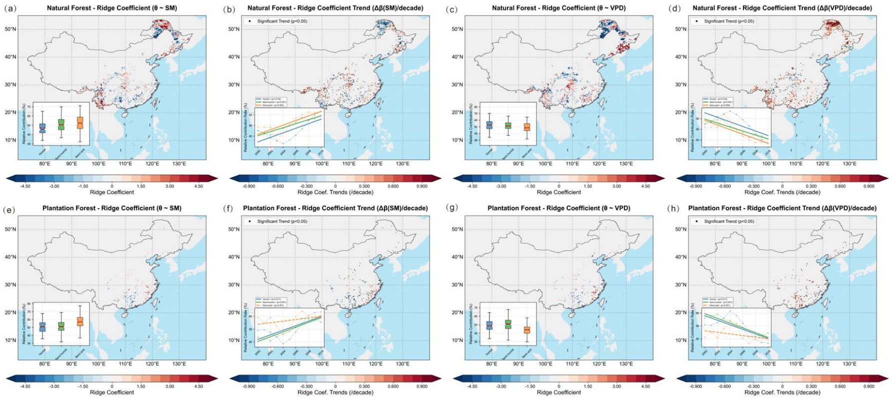

Figure 6 Ridge regression coefficients of forest LAI-TF sensitivity (θ) with SM/VPD and their decadal trends. (a–d for NF, e–h for PF). (a, e) and (c, g) show the spatial distribution of standardized ridge regression coefficients for SM (β_{SM}) and VPD (β_{VPD}), respectively. These coefficients, based on 1995–2015 time series, indicate the independent contribution strength of each factor to θ changes. Inset plots are boxplots of coefficient values for each climatic zone (Humid, Semi-humid, Semi-arid). (b, f) and (d, h) show the temporal trends (decade^{-1}) of β_{SM} and β_{VPD}, respectively. These trends are from Theil-Sen slope estimation and Mann-Kendall tests on the time series of coefficients calculated per-pixel, per-sliding-window. Black dots indicate significant trends ($p < 0.05$). Inset plots show temporal trends of spatially averaged coefficients for each climatic zone (solid for significant, dashed for non-significant).

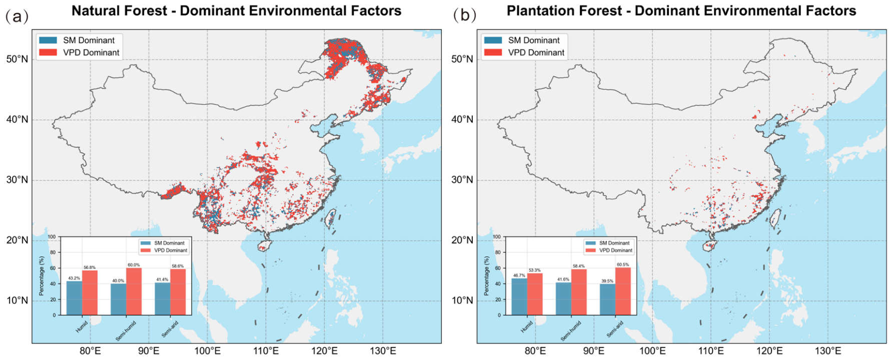

Figure 7 Relative contribution rate of SM/VPD to forest LAI-TF sensitivity (θ). (a) Natural Forest (NF), (b) Planted Forest (PF). For each pixel, the absolute values of ridge regression

coefficients are compared: if $|\beta_{SM}| > |\beta_{VPD}|$, it is SM-dominated (blue); otherwise, VPD-dominated (red). Inset bar charts show the percentage of SM/VPD-dominated area in each arid/humid zone.

The coefficient for SM generally rises, while the coefficient for VPD falls ($\Delta\beta(SM)/decade>0$, $\Delta\beta(VPD)/decade<0$), with most regions reaching significance ($p<0.05$). This "SM↑, VPD↓" direction is consistent across NF, PF, and all three climatic zones, with the change being most pronounced in the semi-arid zone (Fig. 6b,d,f,h inset plots). After determining the dominant factor by relative contribution, VPD-dominant pixels are in the majority nationally, and slightly more so in NF than PF: in NF, the SM/VPD dominance ratios for humid/semi-humid/semi-arid zones are 43.2%/56.8%, 40.0%/60.0%, and 41.4%/58.6%, respectively; for PF, they are 46.7%/53.3%, 41.6%/58.4%, and 39.5%/60.5% (Fig. 7). In NF, the VPD coefficient is more "negative" and has greater dispersion (Fig. S3), especially in the semi-arid zone (lower whisker reaching ~ -6), reflecting a stronger and more unstable inhibitory effect of VPD on θ. SM's median is near 0 to slightly negative, with a narrow distribution. In PF, the medians for both factors are slightly negative, but SM's median and upper quartile are generally higher than VPD's, and the upper whisker is higher in the semi-arid zone, suggesting that in relatively arid afforested areas, the positive (or weakening negative) impact of SM on θ is more easily captured. Overall, the spatial explanation of θ is currently dominated by VPD, but over time, SM's relative role is strengthening while VPD's is weakening. This trend is most significant in the semi-arid zone; meanwhile, the proportion of SM dominance in PF is slightly higher than in NF.

3.3. Attribution of Macro-climate Change Impacts on θ

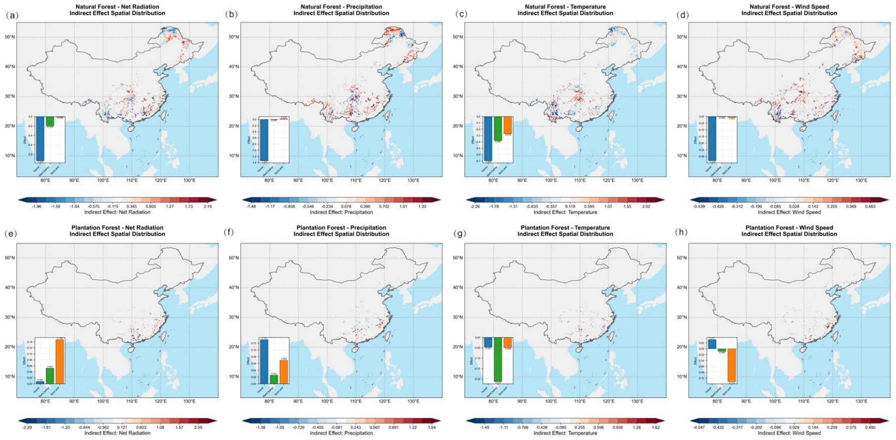

Figure 8 Mediation effects of climate change on forest transpiration sensitivity (θ) via hydrological processes. Natural Forest (NF) and Planted Forest (PF). Spatial distribution of indirect effects from macro-climate factors (Radiation, Precipitation, Temperature, Wind Speed) on θ sensitivity in NF (a-d) and PF (e-h), mediated by local water conditions (SM and VPD). Red (positive) indicates climate change enhances θ via hydrological processes; blue (negative) indicates weakening. Inset plots show the mean indirect effect values for each climatic zone (Humid, Semi-humid, Semi-arid).

To explore the indirect impact of macro-climate factors on θ, we used a mediation effect model to decompose the transmission pathways of climate change via local hydrological processes (SM and VPD). The model's explanatory power (R^2) for θ was 0.39 for NF and 0.35 for PF. Overall, the total indirect effect of climate change on θ was a weak net negative for both NF (mean −0.0163) and PF (mean −0.0125), mainly resulting from the mutual cancellation of stronger, opposing indirect effects from different climate factors. The specific indirect effects of each climate factor show significant spatial heterogeneity, path dependence, and forest type differences (Fig. 8, Fig. 9): Ta is the most consistent negative driver, exerting a negative effect on both forest types in almost all zones, and much stronger in NF (total effect -0.27 to -0.70) than in PF (total effect -0.04 to -0.21). P shows the strongest type differentiation: for PF, P has a positive promotional effect in all zones (total effect +0.02 to +0.13); but for NF, P shows an extremely strong negative inhibition in the humid zone (total effect -1.34), turning slightly positive in the semi-arid zone (+0.02). Rn also shows type differentiation, with a negative effect on NF (especially in the humid zone, total effect -0.93), but a positive effect on PF (especially in the semi-arid zone, total effect +0.14). WS's indirect effect is weakest overall, mainly showing a slight negative effect in the NF humid zone (-0.33) and the PF semi-arid zone (-0.11). Path decomposition (Fig. 9 and detailed data) further reveals the transmission mechanisms: contrary to the initial hypothesis, in the NF humid zone where effects are strongest, the SM path is absolutely dominant. The indirect effects of P (-1.49), Ta (-0.50), Rn (-0.96), and WS (-0.26) are all primarily transmitted via the SM path, while the VPD path effect is relatively weak. The VPD path's dominance is mainly seen in the semi-humid and semi-arid zones; for example, in the NF semi-humid zone, the negative effects of Ta (-0.29) and Rn (-0.24) are contributed mainly by the VPD path. PF's paths are clearer: the positive effects of P and Rn are realized almost entirely through the SM path, while the negative effects of Ta and WS are evident on both SM and VPD paths. Type comparison shows that NF's indirect response to climate drivers (both positive and negative) is much stronger in magnitude than PF's (especially in the humid zone), with the negative effect difference induced by Ta via the VPD path (e.g., semi-humid zone: NF -0.29 vs PF -0.08) being particularly prominent.

Figure 9 Decomposition of indirect effects from Precipitation, Temperature, Radiation, and

https://doi.org/10.5194/egusphere-2025-5821
Preprint. Discussion started: 4 December 2025

Wind Speed on θ in Natural Forests (green) and Planted Forests (brown) via Soil Moisture (SM, solid) and Atmospheric Drought (VPD, hatched) pathways in different climatic zones.

4. Discussion

4.1. Nonlinear Response Characteristics of θ

We found that θ exhibits a significant nonlinear response to the joint SM and VPD gradient, showing a "hump-shaped" pattern nationally (amplified in the middle, attenuated at the extremes), with similar findings on the Tibetan Plateau grasslands (Jin et al., 2023). θ reaches its maximum when SM is at a moderate level and VPD is medium-high; conversely, under extremely humid (high SM, low VPD) or extremely arid (low SM, or super-high VPD) conditions, θ declines significantly (see Fig. 4; Fig. S8, S9). This implies that increasing LAI is most effective at increasing TF in an environment of moderate water supply and evaporative demand (Novick et al., 2016). This nonlinear pattern is highly consistent with plant physiological responses to water supply and atmospheric demand (Liu et al., 2020).

On one hand, at moderate soil water content with some atmospheric drought pressure, vegetation has both sufficient water for transpiration and high atmospheric demand to drive it (Konings et al., 2017). At this "matching" point, the plant hydraulic system is within its safety margin, and stomatal regulation primarily optimizes carbon gain (Sperry et al., 2017), resulting in a high θ.

On the other hand, when the environment deviates from this optimal range, rigid constraints appear, causing θ to decline. When soil is dry or VPD is too high, plants limit water loss via stomatal regulation to avoid sharp declines in water potential, which can lead to xylem embolism and hydraulic failure (McDowell et al., 2022; Sperry et al., 2017). The typical stomatal response to high VPD is partial closure, causing the transpiration rate per unit leaf area to show a nonlinear trend of increasing, then leveling off, or even decreasing at high VPD (Grossiord et al., 2020). This means that even if LAI increases, transpiration rates can hardly increase further under extreme atmospheric drought (Yuan et al., 2019). While rising VPD can promote transpiration within a certain range, stomata begin to close beyond a threshold to reduce excessive water loss, leading to simultaneous suppression of transpiration and photosynthesis (Grossiord et al., 2020). In humid conditions, vegetation transpiration is limited by energy supply and the air's diffusion capacity (i.e., system-atmosphere decoupling) (Konings et al., 2017; Zhou and Yu, 2025). Here, additional leaf area struggles to significantly increase transpiration due to light limitation, poor soil aeration, etc. At the same time, rainfall increases the proportion of Ei and Es (Stoy et al., 2019), which also leads to a decline in TF.

4.2. Long-term Declining Trend of θ

Over the past three decades, θ has shown a significant long-term declining trend (Fig. 3), especially prominent in the semi-arid to semi-humid transition zones. This is consistent with the concurrent meteorological background of rising temperature and VPD, and spatiotemporal redistribution of precipitation and soil moisture (Fig. S5–S7). The "pulling effect" of vegetation greening on TF has generally weakened in recent decades, suggesting a shift in vegetation-water coupling towards a more "water-saving" or "conservative" water-use strategy (Lian et al., 2020). Persistently rising atmospheric CO_2 concentrations have increased plant photosynthetic water use efficiency (iWUE) via the "CO_2 fertilization effect" (Keenan et al., 2016, 2013). Over the past 20+ years, the intrinsic iWUE of temperate and boreal forests in the Northern Hemisphere has significantly increased (Lavergne et al., 2019). This increase is primarily attributed to the partial stomatal closure effect caused by rising CO_2 (Liang et al., 2023; Weiwei et al., 2018). To maintain stable internal CO_2 concentrations, stomata reduce their aperture in high-CO_2 environments, thus lowering water loss per unit leaf area (Keenan et al., 2013). Therefore, vegetation at the same LAI today may support higher photosynthetic carbon assimilation with less transpiration, meaning the transpiration demand per unit leaf area has decreased. This directly leads to a declining trend in θ—because increasing leaf area no longer translates into proportionally higher transpiration rates as it did in the past. This indicates vegetation's water use has become more conservative.

Atmospheric aridification (VPD rise) has shown a global surge since the late 1990s (Grossiord et al., 2020; Yuan et al., 2019). This is due to rising temperatures increasing saturation vapor pressure, while insufficient continental actual vapor supply leads to decreased relative humidity (Yuan et al., 2019). The atmosphere has become drier, and plants more frequently encounter high VPD stress, forcing them into longer periods of stomatal closure or partial closure to avoid transpiration-induced water deficits (Grossiord et al., 2020; Y. Liu et al., 2020). High VPD not only directly suppresses photosynthesis and transpiration rates but has also been found to slow vegetation growth in many regions (Yuan et al., 2019). Yuan et al. (2019) pointed out that the global vegetation "greening" trend slowed significantly after 1998, primarily because the sharp rise in VPD offset the potential promotional effects of CO_2 fertilization. Even if LAI continues to increase, water stress induced by atmospheric drought will limit the transpiration function of additional leaf area, thereby reducing θ. Jin et al. (2023) noted that as the climate turned drier and VPD rose, the amplifying effect of LAI on TF in Tibetan Plateau grasslands significantly weakened, i.e., θ declined over time; θ did not recover even as drought stress continued to intensify. This is consistent with the significant negative trend we identified in the northern semi-arid to semi-humid transition zone (Fig. 3).

4.3. Dynamic Shift of Controlling Factors

Our multi-evidence diagnosis (ridge regression, partial correlation, and mediation path analysis) jointly reveals that during 1990–2020, the key environmental factors controlling θ underwent a gradual shift from the "demand-side" (VPD) to the "supply-side" (SM). Temporally, Fig. 6 shows β_{SM} rising and β_{VPD} falling. Spatially, the partial correlation trends in Fig. 5 also indicate that the negative constraint of $r(\theta, SM \mid VPD)$ is strengthening in most humid and semi-humid pixels, while the negative constraint of $r(\theta, VPD \mid SM)$ is weakening. This "SM constraint strengthening—VPD constraint relatively weakening" evolution does not mean VPD is no longer important. Spatially, VPD-dominated areas are still more widespread (Fig. 7), but under the same background, SM's marginal control on θ is rising. This shift in dominant factors aligns with the macro-context of water supply-demand pattern reshaping under global warming: more regions are transitioning from energy-limited to water-limited (Berg et al., 2016; Denissen et al., 2022), and ecosystem functions are increasingly constrained by soil available water. This widespread shift from energy to water limitation will continue in both time and space, thereby systematically increasing SM's explanatory power for ecosystem transpiration and related processes (Zhou et al., 2019), which is consistent with the signal we captured from θ's temporal change.

The physical picture of this driver shift can be attributed to the dual role of climate warming on the land water cycle. Continuous warming raises saturation vapor pressure and pushes up VPD, increasing potential transpiration demand (Novick et al., 2016; Yuan et al., 2019). However, in the dual environment of high CO_2 and high VPD, vegetation suppresses transpiration through stomatal conservatism and hydraulic risk aversion (Grossiord et al., 2020; McDowell et al., 2022), leading to

https://doi.org/10.5194/egusphere-2025-5821
Preprint. Discussion started: 4 December 2025

a decrease in VPD's marginal drive on θ (i.e., β_{VPD} and r(θ,VPD|SM) weaken). At the same time, the intra-annual/inter-annual redistribution and extremization of precipitation (Fig. S6), coupled with rising Rn and Ta (Fig. S5, S7), cause more regions to cross critical soil moisture thresholds more frequently, entering a water-limited state (Fu et al., 2022; Xu et al., 2019). Once this threshold is crossed, stomatal regulation becomes conservative, VPD's marginal drive is "locked" (Liu et al., 2025), and SM becomes the dominant constraint on θ (Hirschi et al., 2025; Liu et al., 2025). This corresponds exactly to the rising β_{SM} we see in Fig. 6 and the significant downward trend of r(θ, SM|VPD) (negative correlation strengthening) over time in Fig. 5.

From 1990-2020, the rise in β_{SM} and fall in β_{VPD} is a widespread signal, but in terms of spatial extent, VPD-dominant pixels still form the majority—especially in semi-arid/transition zones. This conclusion of a "shift in intensity rather than a replacement of spatial dominance" is consistent with the latest multi-modal evidence: warming continuously increases the *ability* to need water (atmospheric dryness), but the *ability* to access water (effective soil water) is more quickly becoming the bottleneck for E/T (Berg et al., 2016; IPCC, 2023). The result is that θ's elasticity to SM increases, while its independent elasticity to VPD decreases. This is mutually supported by our three sets of evidence from ridge regression, partial correlation, and mediation effects.

4.4. Differences in Response Mechanisms between NF and PF

NF's θ is generally higher, more sensitive to VPD's independent inhibition, and has greater dispersion, while PF's θ has a lower base value, declines faster, and its interannual variability and spatial patterns are more significantly controlled by SM's marginal effect. This differentiation stems first from fundamental differences in community structure and hydraulic strategies. NF is composed of multiple species, ages, and canopy layers, possessing greater hydraulic and trait diversity (Anderegg et al., 2018), including different isohydric/anisohydric control strategies (Martínez-Vilalta and Garcia-Forner, 2017), vulnerability to embolism, and deep-shallow root complementarity (Zhang et al., 2025). NF's structure, on one hand, provides resilience to drought disturbances (Anderegg et al., 2018), and on the other, leads to a stronger stomatal conservative response during high VPD (Grossiord et al., 2020). This manifests in our ridge regression and partial correlations as a larger β_{VPD}, a more negative and dispersed r(θ, VPD|SM) (Fig. 6, Fig. S3), and a relatively flat independent correlation with SM (Fig. 5). Conversely, PF is mostly even-aged, with single or few fast-growing species, simple canopy structure, predominantly shallow roots, and converged hydraulic traits (Farley et al., 2005). This leads to a more significant "synchronous resonance" of community transpiration during surface soil water fluctuations—thus, the negative constraint of r(θ, SM|VPD) is stronger and its decadal strengthening is more prevalent (Fig. 5b, 5f), and the rise in β_{SM} is also more pronounced (Fig. 6f, 6h). This is perfectly consistent with the differences in the nonlinear "peak in the middle, attenuated at the ends" response window we see in Fig. 4: NF's "usable window" is wider (regions of moderate SM × medium-high VPD can better convert LAI increases into TF increases), while PF's window is narrower and attenuates earlier at the extremes (extremely wet or dry, extremely high VPD), indicating its hydraulic safety margin is smaller and it is more sensitive to supply-side deficits (McDowell et al., 2022).

Mediation analysis tells us "who affects θ via which path" (Fig 8–9). In NF humid zones, the negative indirect effects of P, Ta, Rn, and WS on θ are almost all transmitted via the SM path, while the VPD path is relatively minor or opposite in direction. This, on one hand, reflects that under thick canopy conditions, changes in P and Rn more easily amplify canopy interception and soil evaporation, thus "diluting" TF (Chen et al., 2022). On the other hand, it also shows that the combined effect of deep roots, roughness, and litter layer in humid zone NF makes the community insensitive to transient SM deficits, but more sensitive to "energy-turbulence limitation" caused by prolonged wet SM (Huang et al., 2025). In contrast, PF in most zones shows positive indirect effects from P and Rn primarily through the SM path, meaning that once soil water supply improves or canopy transpiration potential is released by increased radiation, PF can quickly convert LAI increases into TF increases; but in phases of negative SM, its θ also decays faster. This runs parallel to the national trend of rising β_{SM} and falling β_{VPD}: spatially, both forest types still have a majority of VPD-dominant pixels, but in terms of intensity, SM's marginal constraint is rising synchronously, and the proportion of SM-dominated area in PF is slightly higher, which aligns perfectly with the "one strengthens, one weakens" partial correlation trend.

NF's "VPD-sensitive, SM-buffered" combination fits its deep-root acquisition and hydraulic diversity (Fan et al., 2017; Zhang et al., 2025): deep roots enhance coupling with groundwater or deep soil water reservoirs, reducing exposure to surface SM fluctuations. But when atmospheric dryness rises to a threshold (Novick et al., 2016), community-wide stomatal conservatism suppresses the transpiration increment per unit LAI (Grossiord et al., 2020), making θ more elastic (negatively) to VPD. At the same time, the thick canopy and rough surface deepen ensemble-layer-atmosphere coupling, making energy/turbulence-limited TF dilution more likely in humid zones (consistent with the "most climate factors → SM path → negative θ effect" in humid zone NF). PF's "SM-sensitive, VPD-relatively-insensitive" stems from its shallow-root, even-aged, trait-convergent nature: any shortage in soil water supply is quickly and synchronously reflected in canopy stomatal conductance and transpiration, causing θ to show a stronger and decadally strengthening negative correlation with SM. In humid situations, once SM and radiation improve, the "rehydration-re-energizing" release for TF is more direct, explaining the positive SM-path effects of P and Rn in most PF zones. Therefore, when we overlay "type difference" with "temporal shift," VPD remains the primary dominant factor explaining θ's current pattern, but in terms of intensity, SM's marginal control is rising (Berg et al., 2016); this rise is faster and more significant in PF. This also implies that under a warming-drying background, NF is more likely to be suppressed in high-VPD years (VPD-dominated stomatal conservatism, θ decline), while PF is more likely to decelerate uniformly when supply bottlenecks appear (SM-dominated threshold crossing), causing θ to fall faster.

Management implications: PF should prioritize enhancing trait and root-depth diversity via mixed-species planting and thinning to reduce synchronous dependence on surface soil water, and configure deeper-rooted or drought-tolerant species in arid-sensitive areas to widen the "effective water window" and reduce threshold-crossing risks (Forrester, 2015). NF should maintain and restore multi-layered canopy structure, roughness, and understory cover to reduce the "dilution" of TF by non-transpiration components (Ei/Es), and alleviate community-scale stomatal stress and hydraulic risk in high-VPD seasons/regions by reducing density to improve ventilation/turbulence coupling. Overall, the conclusion that NF is more constrained by the "atmospheric side" and PF by the "soil side" is consistent with our multi-evidence picture of θ's spatial differentiation, decadal trends, and path decomposition, and provides clear direction for type-based water management in a warming, acidifying background.

5. Conclusion

Based on multi-source data from 1990–2020, this study systematically revealed the spatiotemporal differentiation and hydrological driving mechanisms of LAI-TF sensitivity (θ) in China's NF and PF. Overall, θ spatially increases from humid to semi-arid regions (NF > PF) and temporally shows a widespread significant declining trend (PF decline is larger, mean -0.262 %·m^{-2}·m^{2}·decade^{-1}), especially in ecological transition zones, indicating that the enhancing effect of LAI on TF is systematically weakening. Mechanistically, the controlling factors of θ are undergoing a gradual shift from the "atmospheric demand-side" (VPD) to the "soil supply-side" (SM): although VPD remains the spatially dominant factor (coverage > 50%), its independent control has weakened over time, while SM's has significantly strengthened. Forest type differences are significant: NF (θ higher) is "VPD-sensitive, SM-buffered," showing a stronger response to atmospheric drought; PF (θ lower, declining faster) is "SM-sensitive, VPD-insensitive," showing more sensitivity to soil moisture stress. Mediation analysis confirmed that warming is a consistent negative driver of θ decline, while the effects of precipitation and radiation vary by forest type. China's forests are shifting towards a more "conservative" water-use strategy. This finding provides a scientific basis for climate-adaptive forest management (e.g., type-based root optimization and turbulence enhancement).

Funding

This research was supported by the National Natural Science Foundation of China (Nos. 42277062, 41977149,42230714).

Availability of data and materials

Available on request.

Declaration of Competing Interest

The authors declare that they have no known competing financial interests or personal relationships that could have appeared to influence the work reported in this paper.

References

Anderegg, W.R.L., Konings, A.G., Trugman, A.T., Yu, K., Bowling, D.R., Gabbitas, R., Karp, D.S., Pacala, S., Sperry, J.S., Sulman, B.N., Zenes, N., 2018. Hydraulic diversity of forests regulates ecosystem resilience during drought. Nature 561, 538–541. https://doi.org/10/gd7gjf

Berg, A., Findell, K., Lintner, B., Giannini, A., Seneviratne, S.I., van den Hurk, B., Lorenz, R., Pitman, A., Hagemann, S., Meier, A., Cheruy, F., Ducharne, A., Malyshev, S., Milly, P.C.D., 2016. Land–atmosphere feedbacks amplify aridity increase over land under global warming. Nature Clim Change 6, 869–874. https://doi.org/10/f83mrn

Buck, A.L., 1981. New Equations for Computing Vapor Pressure and Enhancement Factor.

Chen, H., Wei, Y., Huang, J.J., 2024. Widespread increase in plant transpiration driven by global greening. Global and Planetary Change 235, 104395. https://doi.org/10/g9hg5j

Chen, H., Zhu, G., Shang, S., Qin, W., Zhang, Y., Su, Y., Zhang, K., Zhu, Y., Xu, C., 2022. Uncertainties in partitioning evapotranspiration by two remote sensing-based models. Journal of Hydrology 604, 127223. https://doi.org/10/gsm5rt

Cheng, K., Yang, H., Guan, H., Ren, Y., Chen, Y., Chen, M., Yang, Z., Lin, D., Liu, W., Xu, J., Xu, G., Ma, K., Guo, Q., 2024. Unveiling China's natural and planted forest spatial–temporal dynamics from 1990 to 2020. ISPRS Journal of Photogrammetry and Remote Sensing 209, 37–50. https://doi.org/10.1016/j.isprsjprs.2024.01.024

Cheng, K., Zhang, Y., Yang, H., Ren, Y., Xiang, T., Chen, Y., Yang, Z., Chen, M., Xu, J., Huang, G., Xu, G., Tao, S., Yu, Z., Guo, Q., 2025. China's naturally regenerated forests currently have greater aboveground carbon accumulation rates than newly planted forests. Commun Earth Environ 6, 345. https://doi.org/10/hbbn33

Denissen, J.M.C., Teuling, A.J., Pitman, A.J., Koirala, S., Migliavacca, M., Li, W., Reichstein, M., Winkler, A.J., Zhan, C., Orth, R., 2022. Widespread shift from ecosystem energy to water limitation with climate change. Nat. Clim. Change 12, 677–684. https://doi.org/10.1038/s41558-022-01403-8

Fan, Y., Miguez-Macho, G., Jobbágy, E.G., Jackson, R.B., Otero-Casal, C., 2017. Hydrologic regulation of plant rooting depth. Proc. Natl. Acad. Sci. 114, 10572–10577. https://doi.org/10.1073/pnas.1712381114

Farley, K.A., Jobbágy, E.G., Jackson, R.B., 2005. Effects of afforestation on water yield: a global synthesis with implications for policy. Global Change Biology 11, 1565–1576. https://doi.org/10/dk34cg

Forrester, D.I., 2015. Transpiration and water-use efficiency in mixed-species forests versus monocultures: effects of tree size, stand density and season. Tree Physiol 35, 289–304. https://doi.org/10/f7c9tm

Fu, Z., Ciais, P., Feldman, A., Gentine, P., Makowski, D., Prentice, I.C., Stoy, P.C., 2022. Critical soil moisture thresholds of plant water stress in terrestrial ecosystems. Science Advances 8, eabq7827. https://doi.org/10/grrtgr

Grossiord, C., Buckley, T.N., Cernusak, L.A., Novick, K.A., Poulter, B., Siegwolf, R.T.W., Sperry, J.S., McDowell, N.G., 2020. Plant responses to rising vapor pressure deficit. New Phytologist 226, 1550–1566. https://doi.org/10.1111/nph.16485

https://doi.org/10.5194/egusphere-2025-5821
Preprint. Discussion started: 4 December 2025

Hirschi, M., Stradiotti, P., Crezee, B., Dorigo, W., Seneviratne, S.I., 2025. Potential of long-term satellite observations and reanalysis products for characterising soil drying: trends and drought events. Hydrology and Earth System Sciences 29, 397–425. https://doi.org/10/g9976b

Hu, Y., Wei, F., Fu, B., Zhang, W., Sun, C., 2023. Ecosystems in China have become more sensitive to changes in water demand since 2001. Commun Earth Environ 4, 444. https://doi.org/10/hbbnn2

Huang, X., Liang, S., Ziegler, A.D., Zeng, Z., 2025. Decoupling vegetation and soil-moisture interaction in evapotranspiration interannual variability. iScience 28, 113008. https://doi.org/10/hbbn34

Intergovernmental Panel on Climate Change (IPCC) (Ed.), 2023. Weather and Climate Extreme Events in a Changing Climate, in: Climate Change 2021 – The Physical Science Basis: Working Group I Contribution to the Sixth Assessment Report of the Intergovernmental Panel on Climate Change. Cambridge University Press, Cambridge, pp. 1513–1766. https://doi.org/10.1017/9781009157896.013

Jin, Z., You, Q., Zuo, Z., Li, M., Sun, G., Pepin, N., Wang, L., 2023. Weakening amplification of grassland greening to transpiration fraction of evapotranspiration over the Tibetan Plateau during 2001-2020. Agricultural and Forest Meteorology 341, 109661. https://doi.org/10/g9bfk4

Keenan, T.F., Hollinger, D.Y., Bohrer, G., Dragoni, D., Munger, J.W., Schmid, H.P., Richardson, A.D., 2013. Increase in forest water-use efficiency as atmospheric carbon dioxide concentrations rise. Nature 499, 324–327. https://doi.org/10/f449vg

Keenan, T.F., Prentice, I.C., Canadell, J.G., Williams, C.A., Wang, H., Raupach, M., Collatz, G.J., 2016. Recent pause in the growth rate of atmospheric CO2 due to enhanced terrestrial carbon uptake. Nat Commun 7, 13428. https://doi.org/10/f8936d

Koehler, T., Wankmüller, F.J.P., Sadok, W., Carminati, A., 2023. Transpiration response to soil drying versus increasing vapor pressure deficit in crops: physical and physiological mechanisms and key plant traits. J Exp Bot 74, 4789–4807. https://doi.org/10/g8w6qp

Konings, A.G., Williams, A.P., Gentine, P., 2017. Sensitivity of grassland productivity to aridity controlled by stomatal and xylem regulation. Nature Geosci 10, 284–288. https://doi.org/10/f92qx5

Lavergne, A., Graven, H., De Kauwe, M.G., Keenan, T.F., Medlyn, B.E., Prentice, I.C., 2019. Observed and modelled historical trends in the water-use efficiency of plants and ecosystems. Global Change Biology 25, 2242–2257. https://doi.org/10/gf3vmp

Li, C., Han, J., Liu, Z., Tu, Z., Yang, H., 2024. A harmonized global gridded transpiration product based on collocation analysis. Sci Data 11, 604. https://doi.org/10/g9gw9m

Lian, X., Piao, S., Li, L.Z.X., Li, Y., Huntingford, C., Ciais, P., Cescatti, A., Janssens, I.A., Peñuelas, J., Buermann, W., Chen, A., Li, X., Myneni, R.B., Wang, X., Wang, Y., Yang, Y., Zeng, Z., Zhang, Y., McVicar, T.R., 2020. Summer soil drying exacerbated by earlier spring greening of northern vegetation. Sci. Adv. 6, eaax0255. https://doi.org/10.1126/sciadv.aax0255

Liang, X., Wang, D., Ye, Q., Zhang, J., Liu, M., Liu, H., Yu, K., Wang, Y., Hou, E., Zhong, B., Xu, L., Lv, T., Peng, S., Lu, H., Sicard, P., Anav, A., Ellsworth, D.S., 2023. Stomatal responses of terrestrial plants to global change. Nat Commun 14, 2188. https://doi.org/10/gsdfj2

Liu, L., Gudmundsson, L., Hauser, M., Qin, D., Li, S., Seneviratne, S.I., 2020. Soil moisture dominates dryness stress on ecosystem production globally. Nat. Commun. 11, 4892. https://doi.org/10.1038/s41467-020-18631-1

Liu, Y., Kumar, M., Katul, G.G., Feng, X., Konings, A.G., 2020. Plant hydraulics accentuates the effect of atmospheric moisture stress on transpiration. Nat. Clim. Chang. 10, 691–695. https://doi.org/10/gpg5zk

Liu, Y., Lin, Z., Wang, Zijun, Chen, X., Han, P., Wang, B., Wang, Zhenqian, Wen, Z., Shi, H., Zhang, Z., Zhang, W., 2023. Discriminating the impacts of vegetation greening and climate change on the changes in evapotranspiration and transpiration fraction over the Yellow River Basin. Science of The Total Environment 904, 166926. https://doi.org/10/gs264j

Liu, Y., Wang, Y., Zhao, Y., Chen, S., Wang, L., Yang, W., Li, Xing, Li, Xinxi, Lei, H., Chang, H., Zhai, J., Zhu, Y., Wang, Q., Ye, T., 2025. Evapotranspiration stress intensifies with enhanced sensitivity to soil moisture deficits in a rapidly greening China. Hydrology and Earth System Sciences 29, 3379–3404. https://doi.org/10/g9975z

Martínez-Vilalta, J., Garcia-Forner, N., 2017. Water potential regulation, stomatal behaviour and hydraulic transport under drought: deconstructing the iso/anisohydric concept. Plant, Cell & Environment 40, 962–976. https://doi.org/10/gg6k7r

McDowell, N.G., Sapes, G., Pivovaroff, A., Adams, H.D., Allen, C.D., Anderegg, W.R.L., Arend, M., Breshears, D.D., Brodribb, T., Choat, B., Cochard, H., De Cáceres, M., De Kauwe, M.G., Grossiord, C., Hammond, W.M., Hartmann, H., Hoch, G., Kahmen, A., Klein, T., Mackay, D.S., Mantova, M., Martínez-Vilalta, J., Medlyn, B.E., Mencuccini, M., Nardini, A., Oliveira, R.S., Sala, A., Tissue, D.T., Torres-Ruiz, J.M., Trowbridge, A.M., Trugman, A.T., Wiley, E., Xu, C., 2022. Mechanisms of woody-plant mortality under rising drought, CO2 and vapour pressure deficit. Nat Rev Earth Environ 3, 294–308. https://doi.org/10/grz6gb

Niu, Z., He, H., Zhu, G., Ren, X., Zhang, L., Zhang, K., 2020. A spatial-temporal continuous dataset of the transpiration to evapotranspiration ratio in China from 1981–2015. Sci Data 7, 369. https://doi.org/10/gh3225

Novick, K.A., Ficklin, D.L., Stoy, P.C., Williams, C.A., Bohrer, G., Oishi, A.C., Papuga, S.A., Blanken, P.D., Noormets, A., Sulman, B.N., Scott, R.L., Wang, L., Phillips, R.P., 2016. The increasing importance of atmospheric demand for ecosystem water and carbon fluxes. Nature Clim Change 6, 1023–1027. https://doi.org/10/f9dpkn

Qing, Y., Wang, S., Ancell, B.C., Yang, Z.-L., 2022. Accelerating flash droughts induced by the joint influence of soil moisture depletion and atmospheric aridity. Nat Commun 13, 1139. https://doi.org/10/gpp55b

Schlesinger, W.H., Jasechko, S., 2014. Transpiration in the global water cycle. Agricultural and Forest Meteorology 189–190, 115–117. https://doi.org/10/gbfxc6

Song, J., Zhou, S., Yu, B., Li, Y., Liu, Y., Yao, Y., Wang, S., Fu, B., 2024. Serious underestimation of reduced carbon uptake due to vegetation compound droughts. npj Clim Atmos Sci 7, 1–11. https://doi.org/10/gtgssg

Sperry, J.S., Venturas, M.D., Anderegg, W.R.L., Mencuccini, M., Mackay, D.S., Wang, Y., Love, D.M., 2017. Predicting stomatal responses to the environment from the optimization of photosynthetic gain and hydraulic cost. Plant, Cell & Environment 40, 816–830. https://doi.org/10/f9jprm

Stoy, P.C., El-Madany, T.S., Fisher, J.B., Gentine, P., Gerken, T., Good, S.P., Klosterhalfen, A., Liu, S., Miralles, D.G., Perez-Priego, O., Rigden, A.J., Skaggs, T.H., Wohlfahrt, G., Anderson, R.G., Coenders-Gerrits, A.M.J., Jung, M., Maes, W.H., Mammarella, I., Mauder, M., Migliavacca, M., Nelson, J.A., Poyatos, R., Reichstein, M., Scott, R.L., Wolf, S., 2019. Reviews and syntheses: Turning the challenges of partitioning ecosystem evaporation and transpiration into opportunities. Biogeosciences 16, 3747–3775. https://doi.org/10/gf9p7s

Sun, S., Liu, Yibo, Chen, H., Ju, W., Xu, C.-Y., Liu, Yi, Zhou, B., Zhou, Yang, Zhou, Yanlian, Yu, M., 2022. Causes for the increases in both evapotranspiration and water yield over vegetated mainland China during the last two decades. Agricultural and Forest Meteorology 324, 109118. https://doi.org/10/gtcd5n

Wei, Z., Yoshimura, K., Wang, L., Miralles, D.G., Jasechko, S., Lee, X., 2017. Revisiting the contribution of transpiration to global terrestrial evapotranspiration. Geophysical Research Letters 44, 2792–2801. https://doi.org/10/gjkprx

Weiwei, L.U., Xinxiao, Y.U., Guodong, J.I.A., Hanzhi, L.I., Ziqiang, L.I.U., 2018. Responses of Intrinsic Water-use Efficiency and Tree Growth to Climate Change in Semi-Arid Areas of North China. Sci Rep 8, 308. https://doi.org/10/ghvh9v

Xu, H., Yue, C., Zhang, Y., Liu, D., Piao, S., 2023. Forestation at the right time with the right species can generate persistent carbon benefits in China. Proc Natl Acad Sci U S A 120, e2304988120. https://doi.org/10.1073/pnas.2304988120

Xu, L., Chen, N., Zhang, X., 2019. Global drought trends under 1.5 and 2 °C warming. International Journal of Climatology 39, 2375–2385. https://doi.org/10/gh35zt

Yuan, W., Zheng, Y., Piao, S., Ciais, P., Lombardozzi, D., Wang, Y., Liu, Y., Chen, G., Dong, W., Hu, Z., Jain, A.K., Jiang, C., Kato, E., Li, S., Lienert, S., Liu, S., Nabel, J.E.M.S., Qin, Z., Quine, T., Sitch, S., Smith, W.K., Wang, F., Wu, C., Xiao, Z., 2019. Increased atmospheric vapor pressure deficit reduces global vegetation growth. Science Advances 5, eaax1396. https://doi.org/10/gf6gm5

Zahra, N., Hafeez, M.B., Kausar, A., Al Zeidi, M., Asekova, S., Siddique, K.H.M., Farooq, M., 2023. Plant photosynthetic responses under drought stress: Effects and management. Journal of Agronomy and Crop Science 209, 651–672. https://doi.org/10/g9hmkv

Zhang, J., Liu, N., Zhang, C., Zhang, X., He, X., Jiang, W., Li, J., Zhan, Z., Peng, D., Lv, D., Ni, S., 2025. Deep soil moisture has limited impact on mitigating drought stress effects on plant transpiration in a subtropical secondary forest. Plant Soil 514, 427–444. https://doi.org/10/g9bfvc

Zhang, K., Chen, H., Ma, N., Shang, S., Wang, Y., Xu, Q., Zhu, G., 2024. A global dataset of terrestrial evapotranspiration and soil moisture dynamics from 1982 to 2020. Sci Data 11, 1–16. https://doi.org/10.1038/s41597-024-03271-7

Zhou, S., Yu, B., 2025. Neglecting land–atmosphere feedbacks overestimates climate-driven increases in evapotranspiration. Nat. Clim. Chang. 15, 1099–1106.

https://doi.org/10/g93qz7

Zhou, S., Zhang, Y., Park Williams, A., Gentine, P., 2019. Projected increases in intensity, frequency, and terrestrial carbon costs of compound drought and aridity events. Sci. Adv. 5, eaau5740. https://doi.org/10.1126/sciadv.aau5740